Annals of Nuclear Energy 108 (2017) 172–180

Contents lists available at ScienceDirect

Annals of Nuclear Energy

journal homepage: www.elsevier.com/locate/anucene

Improved discrete nodal transport method for treating void regions

Zhitao Xu, Hongchun Wu, Yunzhao Li *, Youqi Zheng

School of Nuclear Science and Technology, Xi'an Jiaotong University, 28 West Xianning Road, Xi'an, Shaanxi 710049, China

ARTICLE INFO

Article history:
Received 2 October 2016
Received in revised form 12 April 2017
Accepted 15 April 2017
Available online 10 May 2017

Keywords:
DNTM
Void regions
NEFD
Nodal
Discrete-ordinates

ABSTRACT

To solve neutron transport problems with void regions accurately and efficiently, the legacy discrete nodal transport method (DNTM) was improved in three-dimensional Cartesian geometry. Firstly, the efficient nodal-equivalent finite difference (NEFD) algorithm was modified, named M-NEFD, to directly treat the zero total cross section in the denominator for void nodes. Furthermore, an angle projection discrete-ordinates (APSN) method was proposed to combine with the NEFD algorithm, named APSN-NEFD, to treat the void regions without sweeping the void nodes one by one. Thirdly, the angular sweeps within one octant of both M-NEFD and APSN-NEFD were parallelized using OpenMP. Based on these improvements, a discrete-ordinates nodal transport code named NECP-HONESTY has been developed in three-dimensional Cartesian geometry. To test the performance of the method and the code, a fission-source problem with two small void regions and a fixed-source problem with one large void region were presented in this paper by comparing with the Monte Carlo method. It has been demonstrated by the numerical results that the improved DNTM can provide accurate eigenvalue and scalar flux, no matter directly sweeping the void nodes with M-NEFD or skipping the void regions with APSN. In addition, compared with M-NEFD, APSN-NEFD can efficiently reduce both computing time and storage requirement for problem with large void regions.

© 2017 Elsevier Ltd. All rights reserved.

1. Introduction

The idea of nodal methods had been implemented in transport theory since late 1970s (Lawrence, 1986). Discrete nodal transport method (DNTM) (Lawrence and Dorning, 1980) is one of the earliest nodal transport methods. It is characterized by the discrete-ordinates (S_N) approximation for angular variables and the nodal transverse-integral approximation for spatial variables. After four decades research and development, it has been improved from different aspects, among which the nodal-equivalent finite difference (NEFD) algorithm (Badruzzaman, 1985) or the weighted diamond-difference form of the nodal transport methods (Walters, 1986; Azmy, 1988) reduce both storage requirement and computing effort efficiently by improving the sweep and iteration strategies. In addition, the anisotropic scattering could be treated by differential scattering cross sections with Legendre polynomials (Wu et al., 1994). It has been implemented in Cartesian (Badruzzaman and Xie, 1984; Azmy, 1988; Wu et al., 1994), hexagonal-Z (Ikeda and Takeda, 1994; Takeda and Yamamoto, 2001) and arbitrary triangular-Z (Lu and Wu, 2007) geometries.

Due to its advantages in computing accuracy and efficiency especially for anisotropic problems, the discrete nodal transport method in arbitrary triangular-Z geometry (Lu and Wu, 2007) has been applied to fast reactor core (Xiao et al., 2015) and accelerator-driven subcritical system (Zhou et al., 2014; He et al., 2015) analyses. However, problem was encountered once void regions appear, such as the FBR core in coolant loss condition and shielding problem with void structures. The singularity of void nodes originated from the NEFD equations due to the appearance of the total cross section in the denominator. Cross sections with small values were used to approximate the zero cross sections for the problem with void regions, which introduces additional errors and is unstable.

In this paper the singularity of void nodes was eliminated by analytically deriving a complete form of the NEFD equations with zero total cross section considered, named modified NEFD (M-NEFD) algorithm. Considering the fact that the angular flux of void nodes is always flat, however, M-NEFD is not economic in the sense of computing time and storage especially for problem with large void regions. As a consequence, a new method, named angle projection discrete-ordinates (APSN) method, was proposed to treat void regions without sweeping them one by one, resulting the APSN-NEFD algorithm. In this method, the angular flux distribution within void regions along each discrete direction is flat and can be

* Corresponding author.
E-mail address: yunzhao@mail.xjtu.edu.cn (Y. Li).

http://dx.doi.org/10.1016/j.anucene.2017.04.048
0306-4549/© 2017 Elsevier Ltd. All rights reserved.

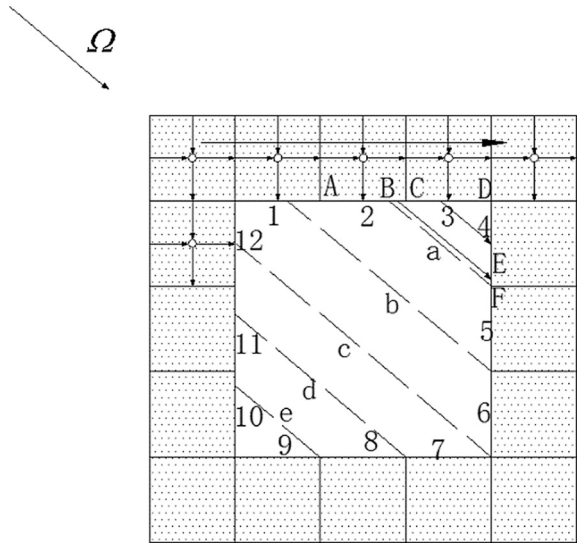

Fig. 1. Illustration of the APSN sweep strategy in 2-D geometry.

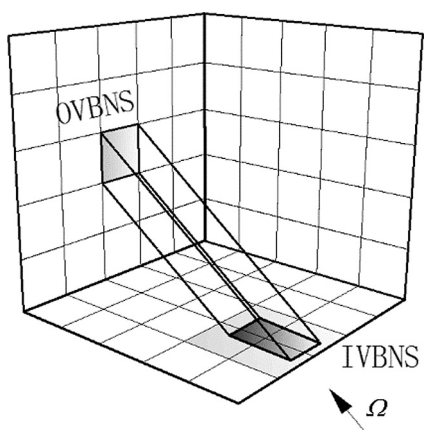

Fig. 2. Illustration of the projection relation in 3-D geometry.

represented by the angular flux on the void-region boundaries. Angular-flux relations between outflow void boundary nodal-surface (OVBNS) and inflow void boundary nodal-surface (IVBNS) are pre-evaluated according to their projection relations before iteratively solving the transport equation. These angular-flux relations are stored as a relation table and will be used to replace nodal sweeps in void regions.

Correspondingly, a discrete-ordinates nodal transport code named NECP-HONESTY (nuclear engineering computational physics laboratory - high order nodal-expansion S_N code for three-dimensional Cartesian geometry) has been developed in three-dimensional Cartesian geometry based on the M-NEFD and APSN-NEFD algorithms. In addition, there is an option to accelerate the process of angular sweeps within one octant by employing the OpenMP platform. It can be used to solve either fission- or fixed-source problem. Anisotropic scattering, high order interior flux and source can also be handled.

Basic theory and analyses of M-NEFD and APSN-NEFD will be presented in Section 2. In Section 3, a fission-source problem with two small void regions and a fixed-source problem with one large void region will be presented to verify the improvements. Section 4 gives the conclusions of this paper.

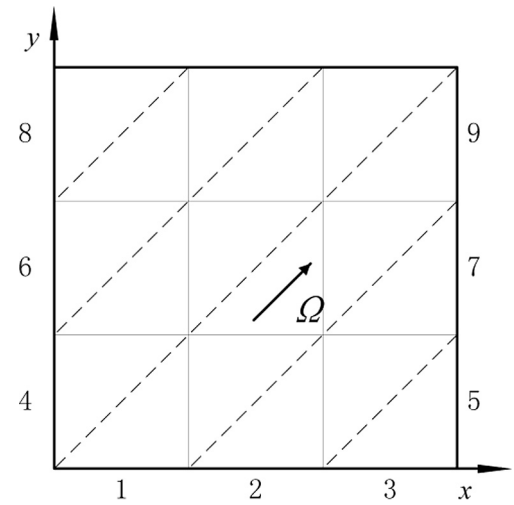

Fig. 3. Illustration of a 2-D void region.

2. Theory

After the classic DNTM is briefly introduced in Section 2.1, the M-NEFD equations will be given in Section 2.2, while the theory of APSN-NEFD will be introduced in Section 2.3. Section 2.4 compares M-NEFD and APSN-NEFD. The parallelization using OpenMP within one octant will be explained in Section 2.5.

2.1. The classic DNTM

Multi-group neutron transport equation in a cuboid node is as following,

$$\frac{2\mu}{\Delta x}\frac{\partial\varphi_g}{\partial x}+\frac{2\eta}{\Delta y}\frac{\partial\varphi_g}{\partial y}+\frac{2\xi}{\Delta z}\frac{\partial\varphi_g}{\partial z}+\Sigma_{t,g}\varphi_g=S_g,\quad -1\leqslant x,y,z\leqslant 1, \tag{1}$$

where μ, η and ξ are direction cosines relative to x, y and z axes respectively in 3-D Cartesian geometry, Δx, Δy and Δz are nodal dimensions (cm), g indexes the energy group, neutron flux φ_g ($\mathrm{cm^{-2}\cdot s^{-1}}$) is a function of μ, η, ξ, x, y and z, while $\Sigma_{t,g}$ refers to the total cross section ($\mathrm{cm^{-1}}$), and S_g stands for the neutron source ($\mathrm{cm^{-3}\cdot s^{-1}}$).

Transverse-integral equation in x channel can be obtained by integrating Eq. (1) over y and z channels:

$$\frac{2\mu}{\Delta x}\frac{\partial\varphi_x}{\partial x}+\Sigma_t\varphi_x=S_x-L_x, \tag{2}$$

where

$$\varphi_x=\int_{-1}^{1}\int_{-1}^{1}\varphi(x,y,z)dydz\Big/\int_{-1}^{1}\int_{-1}^{1}dydz, \tag{3}$$

$$S_x=\int_{-1}^{1}\int_{-1}^{1}S(x,y,z)dydz\Big/\int_{-1}^{1}\int_{-1}^{1}dydz, \tag{4}$$

$$L_x=L_{\bar{y}x}+L_{\bar{z}x}, \tag{5}$$

and L_x is the transverse leakage term for x channel. Note that the energy group index g is omitted for simplification.

Taking $\varphi_x(-1)$ as a known value for $\mu>0$, Eq. (2) can be solved analytically:

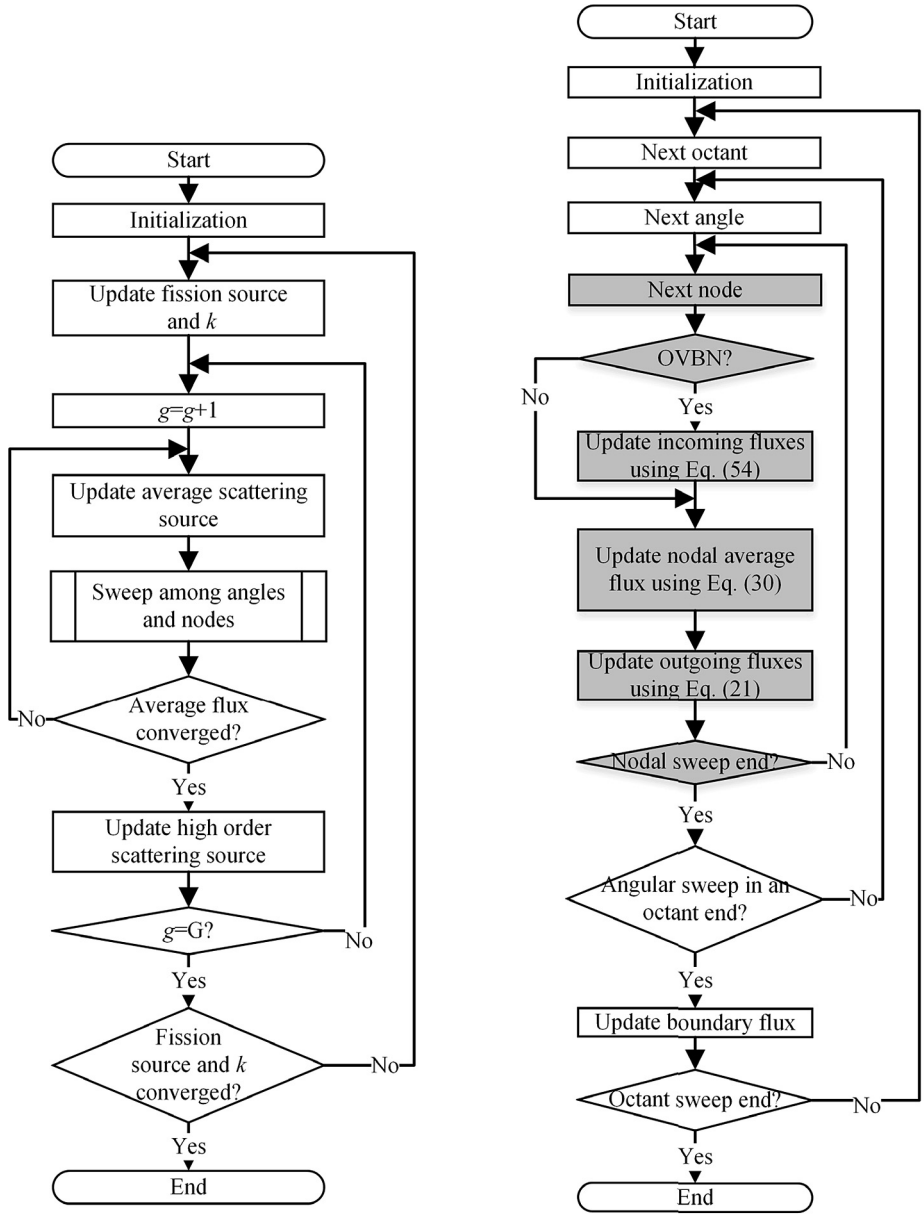

(a) Flowchart of source iterations (b) Flowchart of angular and nodal sweeps

Fig. 4. Iteration and sweep flowchart.

$$\varphi_x(x) = \varphi_x(-1)\mathrm{E}(x+1) + \frac{\Delta x}{2\mu}\mathrm{E}(x)\int_{-1}^{x}[S_x(x') - L_x(x')]\mathrm{E}(-x')dx', \quad \mu > 0, \tag{6}$$

where

$$\mathrm{E}(x) = \exp\left(-\frac{\Sigma_t \Delta x}{2\mu}x\right). \tag{7}$$

The expression of $\varphi_x(1)$ can be obtained from Eq. (6):

$$\varphi_x(1) = \varphi_x(-1)\mathrm{E}(2) + \frac{\Delta x}{2\mu}\mathrm{E}(1)\int_{-1}^{1}[S_x(x') - L_x(x')]\mathrm{E}(-x')dx', \mu > 0. \tag{8}$$

Approximating spatial variables with Legendre polynomials yields

$$\varphi_x(x) = \sum_{n=0}^{N}\frac{2n+1}{2}\varphi_{xn}P_n(x), \tag{9}$$

$$S_x(x) = \sum_{n=0}^{NS}\frac{2n+1}{2}S_{xn}P_n(x), \tag{10}$$

$$L_x(x) = \sum_{n=0}^{NL}\frac{2n+1}{2}L_{xn}P_n(x), \tag{11}$$

with

$$\varphi_{xn} = \int_{-1}^{1}\varphi_x(x)P_n(x)dx, \tag{12}$$

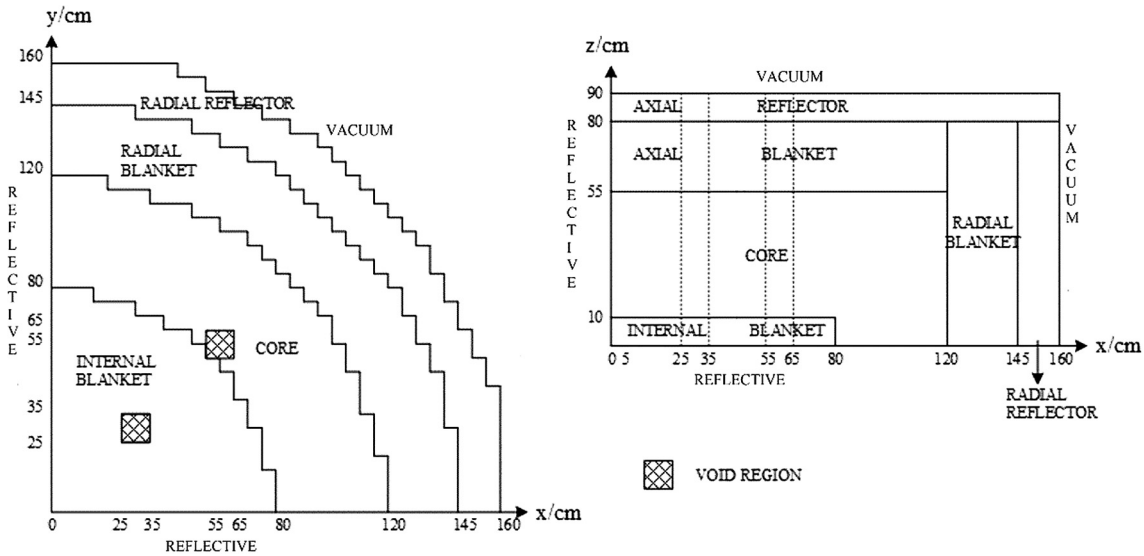

Fig. 5. Configuration of the axially heterogeneous FBR core.

Table 1
Results of the axially heterogeneous FBR core.

Method	Eigenvalue		Time used/s	Storage/MB
	Value	Percent error		
Monte Carlo	1.01398	±0.003	–	–
M-NEFD	1.01315	−0.082	33.3	41
APSN-NEFD	1.01405	0.007	32.8	41

Table 2
Region-averaged flux results of the axially heterogeneous FBR core.

Region		Monte Carlo		M-NEFD		APSN-NEFD	
		Flux ($cm^{-2}\,s^{-1}$)	Statistical error (%)	Flux ($cm^{-2}\,s^{-1}$)	Error (%)	Flux ($cm^{-2}\,s^{-1}$)	Error (%)
Internal blanket	1G	1.2258×10^{-5}	0.04	1.2299×10^{-5}	0.34	1.2326×10^{-5}	0.56
	2G	1.1076×10^{-4}	0.02	1.1018×10^{-4}	−0.52	1.1048×10^{-4}	−0.26
	3G	1.1814×10^{-4}	0.02	1.1749×10^{-4}	−0.55	1.1792×10^{-4}	−0.19
	4G	7.0838×10^{-6}	0.06	7.0513×10^{-6}	−0.46	7.0785×10^{-6}	−0.07
Core	1G	1.9449×10^{-5}	0.01	1.9446×10^{-5}	−0.01	1.9429×10^{-5}	−0.10
	2G	1.1209×10^{-4}	0.01	1.1217×10^{-4}	0.07	1.1214×10^{-4}	0.05
	3G	8.1350×10^{-5}	0.01	8.1285×10^{-5}	−0.08	8.1346×10^{-5}	−0.01
	4G	3.2406×10^{-6}	0.03	3.2350×10^{-6}	−0.17	3.2384×10^{-6}	−0.07
Radial blanket	1G	1.4341×10^{-6}	0.05	1.4378×10^{-6}	0.26	1.4344×10^{-6}	0.02
	2G	1.5290×10^{-5}	0.02	1.5296×10^{-5}	0.04	1.5268×10^{-5}	-0.14
	3G	1.9846×10^{-5}	0.02	1.9860×10^{-5}	0.07	1.9828×10^{-5}	−0.09
	4G	1.6558×10^{-6}	0.05	1.6588×10^{-6}	0.18	1.6562×10^{-6}	0.02
Axial blanket	1G	2.8298×10^{-6}	0.04	2.8427×10^{-6}	0.46	2.8441×10^{-6}	0.51
	2G	2.9291×10^{-5}	0.02	2.9238×10^{-5}	−0.18	2.9224×10^{-5}	−0.23
	3G	3.4418×10^{-5}	0.02	3.4378×10^{-5}	−0.12	3.4323×10^{-5}	−0.28
	4G	3.5690×10^{-6}	0.04	3.5647×10^{-6}	−0.12	3.5551×10^{-6}	−0.39

$$S_{xn} = \int_{-1}^{1} S_x(x) P_n(x) dx, \tag{13}$$

$$L_{xn} = \int_{-1}^{1} L_x(x) P_n(x) dx, \tag{14}$$

where N, NS and NL are the expansion orders of flux, source and transverse leakage terms respectively. In this paper, only $NL = 0$ is considered. Substituting Eqs. (9)–(11) in Eq. (8), the outgoing surface-flux becomes:

$$\varphi_x(1) = \varphi_x(-1)E(2) + \sum_{n=0}^{NS} F_{xn+} S_{xn} - F_{x0+} L_{x0}, \mu > 0, \tag{15}$$

where

$$F_{xn+} = \frac{\Delta x}{2\mu} \frac{2n+1}{2} E(1) \int_{-1}^{1} P_n(x) E(-x) dx, \tag{16}$$

$$L_{x0} = \frac{2\xi}{\Delta z}[\varphi_z(1) - \varphi_z(-1)] + \frac{2\eta}{\Delta y}[\varphi_y(1) - \varphi_y(-1)], \tag{17}$$

and the sign + in F_{xn+} means that the coefficient F_{xn+} is for $\mu > 0$. Substituting Eqs. (9)–(11) in Eq. (6) and using the orthogonality of Legendre polynomials, the nodal interior flux moment is obtained as:

$$\varphi_{xk} = \varphi_x(-1)G_{xk+} + \sum_{n=0}^{NS} G_{xkn+}S_{xn} - G_{xk0+}L_{x0}, \quad k = 0, 1, \ldots, N, \mu > 0, \tag{18}$$

where

$$G_{xk+} = \int_{-1}^{1} E(x+1)P_k(x)dx, \tag{19}$$

$$G_{xkn+} = \frac{\Delta x}{2\mu}\frac{2n+1}{2}\int_{-1}^{1} E(x)[\int_{-1}^{x} P_n(x')E(-x')dx']P_k(x)dx. \tag{20}$$

The M-NEFD equations will be derived based on the above classical DNTM equations.

2.2. The M-NEFD algorithm

Eliminating S_{x0} in Eq. (15) with Eq. (18) when $k = 0$, one obtains

$$\varphi_x(1) = (1 - A_{x+})\varphi_x(-1) + B_{x+}\overline{\varphi} + \sum_{n=1}^{NS} C_{xn+}S_{xn}, \mu > 0, \tag{21}$$

where

$$A_{x+} = -E(2) + \frac{F_{x0+}(1)G_{x0+}}{G_{x00+}} + 1, \tag{22}$$

$$B_{x+} = \frac{2F_{x0+}(1)}{G_{x00+}}, \tag{23}$$

$$C_{xn+} = F_{xn+}(1) - \frac{F_{x0+}(1)G_{x0n+}}{G_{x00+}}. \tag{24}$$

Eliminating S_{x0} in Eq. (18) when $k > 0$ with Eq. (18) when $k = 0$, one obtains

$$\varphi_{xk} = U_{xk+}\varphi_x(-1) + V_{xk+}\overline{\varphi} + \sum_{n=1}^{NS} W_{xkn\pm}S_{xn}, \quad k = 1, 2, \ldots, N, \mu > 0, \tag{25}$$

where

$$U_{xk+} = \left(G_{xk+} - \frac{G_{xk0+}G_{x0+}}{G_{x00+}}\right), \tag{26}$$

$$V_{xk+} = \frac{2G_{xk0+}}{G_{x00+}}, \tag{27}$$

$$W_{xkn+} = G_{xkn+} - \frac{G_{xk0+}G_{x0n+}}{G_{x00+}}. \tag{28}$$

Eqs. (21) and (25) form the nodal response relation in x channel when $\mu > 0$. Similar equations can be obtained for x channel with $\mu < 0$, for y channel with $\eta > 0$ or $\eta < 0$, and for z channel with $\xi > 0$ or $\xi < 0$.

Integrating Eq. (1) over x, y and z channel, neutron balance equation in one node is obtained:

$$\frac{\mu}{\Delta x}[\varphi_x(1) - \varphi_x(-1)] + \frac{\eta}{\Delta y}[\varphi_y(1) - \varphi_y(-1)] + \frac{\xi}{\Delta z}[\varphi_z(1) - \varphi_z(-1)] + \Sigma_t\overline{\varphi} = \overline{S}. \tag{29}$$

Eliminating the outgoing surface-fluxes in Eq. (29) with Eq. (21) and it's counterparts for other combinations of cosines and channels, one obtains

$$\overline{\varphi} = \left\{\overline{S} + \frac{|\mu|}{\Delta x}[A_x\varphi_x(f_\mu) - \sum_{n=1}^{NS} C_{xn}S_{xn}] + \frac{|\eta|}{\Delta y}\left[A_y\varphi_y(f_\eta) - \sum_{n=1}^{NS} C_{yn}S_{yn}\right] + \frac{|\xi|}{\Delta z}\left[A_z\varphi_z(f_\xi) - \sum_{n=1}^{NS} C_{zn}S_{zn}\right]\right\} \Big/ \left(\frac{|\mu|}{\Delta x}B_x + \frac{|\eta|}{\Delta y}B_y + \frac{|\xi|}{\Delta z}B_z + \Sigma_t\right), \tag{30}$$

where

$$f_v = -\mathrm{sgn}\, v, v = \mu, \eta, \xi, \tag{31}$$

A_u $(u = x, y, z)$ equals to $A_{u\pm}$ with the sign $\pm$ determined the by f_v, and the same rule suits for B_u and C_{nu}, and sgn is the signum function.

For a given neutron flux direction (μ, η, ξ), nodal-sweep sequence is ensured by the continuous conditions between adjacent nodes and boundary conditions. For a given node and a given direction, three incoming surface-fluxes are known while three outgoing surface-fluxes are intended to be updated. The nodal average flux is computed first with Eq. (30). Then the outgoing surface-fluxes are computed with Eq. (21) and it's counterparts. High order flux moments are updated with Eq. (25) and it's counterparts after the nodal average scattering-source iteration.

Method to obtain the complete form of the related integration coefficients will be given as below. Legendre polynomials can be written as following:

$$P_n(x) = \sum_{n'=0}^{n} p_{n'-n}x^{n'}, \tag{32}$$

where $p_{n'-n}$ refers to the coefficient of orthogonal polynomials. Substituting Eq. (32) in Eq. (16), (19) and (20) respectively, the coefficients for x channel and $\mu > 0$ are reformulated as below:

$$F_{xn+} = b_x c_x(n + 0.5)\sum_{n'=0}^{n} p_{n'-n}I_{n'}^{a_x}, \tag{33}$$

$$G_{xk+} = c_x\sum_{k'=0}^{k} p_{k'-k}I_{k'}^{-a_x}, \tag{34}$$

$$G_{xkn+} = b_x(n + 0.5)\sum_{n'=0}^{n}\sum_{k'=0}^{k} p_{n'-n}p_{k'-k}J_{k'n'}, \tag{35}$$

where

$$b_x = \frac{\Delta x}{2|\mu|}, \tag{36}$$

$$a_x = \Sigma_t b_x, \tag{37}$$

$$c_x = e^{-a_x}, \tag{38}$$

$$I_{n'}^{a_x} = \int_{-1}^{1} x^{n'}e^{a_x x}dx, \tag{39}$$

$$I_{k'}^{-a_x} = \int_{-1}^{1} x^{k'}e^{-a_x x}dx, \tag{40}$$

$$J_{k'n'} = \int_{-1}^{1} x^{k'}e_{xx}^{-a}\left(\int_{-1}^{x} x^{m'}e^{a_x x'}dx'\right)dx. \tag{41}$$

After mathematical simplifications, one can obtain the complete form of the integrations $I_n^{a_x}$ and J_{kn} as following:

$$I_n^{a_x} = (-1)^{n+1} e^{a_x} \sum_{l=0}^{n} \frac{(-1)^{l+1}}{a_x^{n-l+1}} \frac{n!}{l!} + (-1)^{n+1} e^{-a_x} \sum_{l=0}^{n} \frac{1}{a_x^{n-l+1}} \frac{n!}{l!}, a_x > 0, \tag{42}$$

$$I_n^{a_x} = \begin{cases} 2, & n = 0 \\ 0, & n > 0 \end{cases}, \quad a_x = 0, \tag{43}$$

$$I_n^{-a_x} = (-1)^n I_n^{a_x}, \tag{44}$$

$$J_{kn} = (-1)^{n+1} \sum_{l=0}^{n} \frac{(-1)^{l+1}}{a_x^{n-l+1}} \frac{n!}{l!} \frac{1-(-1)^{l+k+1}}{l+k+1} + (-1)^{n+1} e^{-a_x} I_k^{-a_x} \sum_{l=0}^{n} \frac{1}{a_x^{n-l+1}} \frac{n!}{l!}, a_x > 0, \tag{45}$$

$$J_{kn} = \begin{cases} 4, & k+n = 0 \\ 0, & k+n > 0 \end{cases}, \quad a_x = 0 \tag{46}$$

And the recursion form of the integrations as following:

$$I_0^{a_x} = (e^{a_x} - e^{-a_x})/a_x, a_x > 0, \tag{47}$$

$$I_n^{a_x} = -\frac{n}{a_x} I_{n-1}^{a_x} + (e^{a_x} + (-1)^{n+1} e^{-a_x})/a_x, a_x > 0, \tag{48}$$

$$J_{k0} = \left[\frac{1-(-1)^{k+1}}{k+1} - e^{-a_x} I_k^{-a_x} \right] / a_x, a_x > 0, \tag{49}$$

$$J_{kn} = -\frac{n}{a_x} I_{k(n-1)} + \left[\frac{1-(-1)^{n+k+1}}{n+k+1} + (-1)^{n+1} e^{-a_x} I_k^{-a_x} \right] / a_x, a_x > 0. \tag{50}$$

The relations between the coefficients for $\mu < 0$ and the coefficients for $\mu > 0$ are as following:

$$F_{xn-} = (-1)^n F_{xn+}, \tag{51}$$

$$G_{xk-} = (-1)^k G_{xk+}, \tag{52}$$

$$G_{xkn-} = (-1)^{k+n} G_{xkn+}. \tag{53}$$

Similar formulas can be obtained for y and z channels. For void nodes with $a = 0$, the integration coefficients were obtained using Eqs. (43) and (46) instead of Eqs. (42) and (45), the M-NEFD equations still hold.

2.3. The APSN-NEFD algorithm

In this subsection, a new S_N sweep strategy which eliminates the nodal sweeps in large void regions is given and results the APSN-NEFD algorithm when combined with the NEFD equations. For a given direction $\mathbf{\Omega}$, non-void nodes are swept one by one according to their adjacent relationships. For void nodes, the incoming surface-fluxes of a node equal to the outgoing surface-fluxes of its adjacent nodes or can be determined by the boundary conditions. However, in the APSN method, the incoming surface-flux of one node could be determined by the outgoing surface-fluxes of several void boundary nodes. As illustrated in Fig. 1, in a 2-D model with one void region, the incoming flux of surface 4 is determined by a part of the outgoing flux of surface 2 and the outgoing flux of surface 3, the incoming flux of surface 5 is determined by parts of the outgoing fluxes of surface 1 and surface 2.

According to the neutron balance principle, the relation between one OVBNS flux and several IVBNS fluxes for constant surface-flux approximation can be derived as below:

$$\varphi_o = \sum_{m=1}^{M} \varphi_{i_m} \omega_{i_m-o}^{\mathbf{\Omega}}, \tag{54}$$

$$\omega_{i_m-o}^{\mathbf{\Omega}} = \frac{\mathbf{r}_{i_m} \cdot \mathbf{\Omega}}{\mathbf{r}_o \cdot \mathbf{\Omega}} \frac{\Delta S_{i_m-o}}{\Delta S_o}, \tag{55}$$

where φ_o is the OVBNS flux, M is the total number of IVBNS related to φ_o according to the angle projection relations, φ_{i_m} is the mth IVBNS flux, $\omega_{i_m-o}^{\mathbf{\Omega}}$ is the weight of φ_{i_m} to φ_o in the direction of $\mathbf{\Omega}$, $\mathbf{r}_{i_m}$ is the normal vector of the mth IVBNS, $\mathbf{r}_o$ is the normal vector of the OVBNS, $\mathbf{\Omega}$ is the unit vector of a discrete direction, ΔS_{i_m-o} is the area of the part that neutron can reach the OVBNS from the mth IVBNS, ΔS_o is the area of the OVBNS.

A relation table can be pre-evaluated by angle-projection relations to store all the weights $\omega_{i_m-o}^{\mathbf{\Omega}}$ before nodal sweeps. The algorithm to get the relation table involves the knowledge of computational geometry (Preparata and Shamos, 1985) and can be vital for the computing efficiency. For a given OVBNS and a given $\mathbf{\Omega}$, if an IVBNS overlaps the projection of this OVBNS along the direction $\mathbf{\Omega}$, this IVBNS is related to the OVBNS and the overlap area and the weight can be calculated by using Eq. (55). As illustrated in Fig. 2, the projection of one OVBNS overlaps four IVBNS, four times polygon overlap calculations are needed.

2.4. Comparison of M-NEFD and APSN-NEFD

The accuracies of both M-NEFD and APSN-NEFD can be separated into two parts, namely the void regions and the non-void regions. For non-void regions, the accuracy depends on the spatial and angular discretization, which is the same for the two algorithms. In contrast, for void regions, their spatial and angular discretization is different. For convenience the following discussions will consider the case of 2-D geometry with $\mu > 0$ and $\eta > 0$, but the conclusion maintain valid for other cases.

First consider the spatial discretization errors of the two algorithms in void regions. Since Eq. (54) is derived using the neutron balance principle, the void-region spatial discretization error of APSN-NEFD is determined only by the void boundary nodal-surface (VBNS) discretization error which depends on the spatial discretization in non-void regions. In contrast, void-nodal sweeps in M-NEFD causes additional error. In one void node, Eq. (30) becomes

$$\overline{\varphi} = \mu' \varphi_x(-1) + \eta' \varphi_y(-1), \tag{56}$$

where

$$\mu' = \frac{|\mu|\Delta y}{|\mu|\Delta y + |\eta|\Delta x}, \tag{57a}$$

$$\eta' = \frac{|\eta|\Delta x}{|\mu|\Delta y + |\eta|\Delta x}, \tag{57b}$$

$$\mu' + \eta' = 1. \tag{57c}$$

Meanwhile, Eq. (21) becomes

$$\varphi_x(1) = \overline{\varphi}. \tag{58}$$

Substituting Eq. (56) in Eq. (58) and it's counterpart in y channel, the outgoing surface-flux given by M-NEFD is:

$$\varphi_x(1) \equiv \varphi_y(1) = \mu' \varphi_x(-1) + \eta' \varphi_y(-1). \tag{59}$$

$\varphi_x(1) \equiv \varphi_y$ means that there is a flux-averaging effect in one void node, which will induce approximation. However, for APSN-NEFD, Eq. (54) gives

$$\varphi_x(1) = \begin{cases} (1-\eta'/\mu')\varphi_x(-1) + (\eta'/\mu')\varphi_y(-1), & \mu' > \eta' \\ \varphi_y(-1), & \mu' \leqslant \eta' \end{cases} \tag{60a}$$

$$\varphi_y(1) = \begin{cases} \varphi_x(-1), & \eta' \leqslant \mu' \\ (1-\mu'/\eta')\varphi_y(-1) + (\mu'/\eta')\varphi_x(-1), & \eta' > \mu' \end{cases} \tag{60b}$$

Eqs. (60a) and (60b) are derived considering the neutron flight law in the void node and with no additional approximation induced. Thus the error caused by flux-averaging effect of M-NEFD in one void node can be evaluated by subtracting Eqs. (60a) and (60b) from Eq. (59) respectively. Considering x channel:

$$\Delta\varphi_x(1) = \begin{cases} (\mu' + 1/\mu' - 2)[\varphi_x(-1) - \varphi_y(-1)], & 0.5 < \mu' \leqslant 1 \\ \mu'[\varphi_x(-1) - \varphi_y(-1)], & 0 \leqslant \mu' \leqslant 0.5 \end{cases}. \tag{61}$$

$\Delta\varphi_x(1)$ will be non-zero except when $\mu' = 0$ or $\mu' = 1$ and can be maximal when $\mu' = \eta'$, which are also true for $\Delta\varphi_y(1)$. For a void region with multiple void nodes, the error will be accumulated.

Then the angular discretization errors of the two algorithms in void regions can also be analyzed. Both of the two algorithms deal the angular variables with S_N method which approximates the angular variables with limited number of directions. The S_N method causes obvious flux distribution error and fluctuation when the spatial singularity of source term (including possible fission source, scattering source and external source) in Eq. (1) is significant, namely the ray effect. For problem with void regions, there is no source except on the void boundary, which enhances the ray effect for both M-NEFD and APSN-NEFD.

However, for M-NEFD the flux-averaging effect sometimes can cancel out part of the ray effect. Taking a 2-D void region with nine void nodes illustrated in Fig. 3 as an example and supposing only one discrete direction $\mathbf{\Omega}$ is used in the $(x > 0, y > 0)$ octant to approximate the angular variables, for APSN-NEFD the neutrons in surface 2 can't reach surface 5 and surface 9, which exposes the ray effect; while for M-NEFD the neutrons in surface 2 can reach surface 5, surface 7 and surface 9 as illustrated by the following equations derived with Eq. (59),

$$\varphi_5 = \mu'^3\varphi_4 + \mu'^2\eta'\varphi_1 + \mu'\eta'\varphi_2 + \eta'\varphi_3, \tag{62}$$

$$\varphi_7 = 3\mu'^2\eta'^2\varphi_1 + 2\mu'\eta'^2\varphi_2 + \eta'^2\varphi_3 + 3\mu'^3\eta'\varphi_4 + \mu'^3\varphi_6, \tag{63}$$

$$\varphi_9 = 6\mu'^2\eta'^3\varphi_1 + 3\mu'\eta'^3\varphi_2 + \eta'^3\varphi_3 + 6\mu'^3\eta'^2\varphi_4 + 3\mu'^3\eta'\varphi_6 + \mu'^3\varphi_8. \tag{64}$$

Actually, neutrons in surface 2 will reach surface 5 or surface 9 along a direction different from $\mathbf{\Omega}$ if without the ray effect, which means the error cancelation between the flux-averaging effect and the ray effect is not a certainty.

As a conclusion, the accuracy of M-NEFD is determined by the ray effect and the flux-averaging effect in the void region plus the spatial and angular discretization in the non-void region; while there is no flux-averaging effect in APSN-NEFD with only the ray effect in the void region plus the spatial and angular discretization in the non-void region.

2.5. The angular parallelization using OpenMP

Different angles in each octant of either M-NEFD or APSN-NEFD can be separated in threading. Thus, OpenMP was employed to parallelize them. The flowchart of fission-source (only for fission-source problem) and scattering-source iterations is illustrated in Fig. 4(a). The iteration process stops once both the maximum errors of scattering and fission sources and the error of eigenvalue k between two adjacent iterations satisfy the predefined criterion. The flowchart of angular and spatial sweeps to update nodal average scattering source of the gth energy group is illustrated in Fig. 4(b). The steps with gray background in Fig. 4(b) are paralleled using the shared-memory programming model of OpenMP.

The ideal speedup of the shared-memory parallelization is determined by the *Amdahl's law* (Chapman et al., 2007) as below:

$$S = \frac{1}{(f_{par}/P + (1 - f_{par}))}, \tag{65}$$

where f_{par} is the parallel fraction of the code and P is the number of processors. And the parallel efficiency is defined as:

$$E = S/P. \tag{66}$$

From Eqs. (65) and (66), it can be seen that the speedup and parallel efficiency are ideal for large problem with f_{par} approximate to 1. Actually, the speedup and parallel efficiency will be less because extra CPU time is needed to create, start, stop and manage the threads for parallel regions.

3. Results

A code named NECP-HONESTY was developed with both M-NEFD and APSN-NEFD included for void regions in 3-D Cartesian geometry. To simplify the complex geometry computation in void regions of APSN-NEFD, only cuboid void regions was considered in the code. Several cuboid void regions can be set to approximate each complex void region. Numerous numerical tests have been carried out with one fission-source problem with two small void regions and one fixed-source problem with one large void region presented in this paper. Reference solutions were provided by a Monte Carlo code.

3.1. A fission-source problem with two small void regions

This is a variant of the axially heterogeneous FBR core (model 3) in the NEACRP 3-D neutron transport benchmarks (Takeda and Ikeda, 1991). The 1/8 core configuration is illustrated in Fig. 5. The geometry and cross sections are the same as those of the model 3. Different from model 3, two control rods are replaced with two void regions.

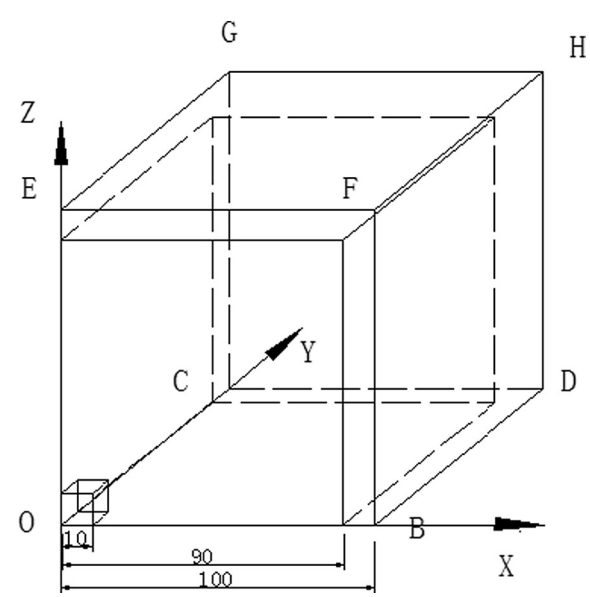

Fig. 6. Geometry of the fixed-source problem.

Table 3
Results of the fixed-source problem.

Method	Region-averaged flux/cm^{-2}·s^{-1}		CPU[b] Time/s			Storage
	Source	Shield	Total	Iteration	Setup	/GB
Monte Carlo	7.066 0.01[a]	2.742×10^{-2} 0.01	–	–	–	–
M-NEFD	7.068 0.03	2.756×10^{-2} 0.51	637.8	636.2	0.3	11.9
APSN-NEFD	7.068 0.03	2.745×10^{-2} 0.11	300.3	219.8	79.9	4.8

[a] Percent error.
[b] Intel® Xeon® CPU E5-2620 @ 2.10 GHz.

S_4 Legendre-Chebyshev quadrature was used, the expansion order of interior flux and source are both 2. The nodal dimensions are 5 cm in both *x* and *y* directions, while the nodal dimensions in *z* direction from the bottom to the top are 5, 5, 9, 9, 9, 9, 9, 8, 8, 9 and 10 cm. Three CPU processors (Intel® Xeon® CPU E5-2620 @ 2.10 GHz) were used. About 88% parallel efficiency is obtained for this problem. Table 1 displays the results of calculated eigenvalue and their errors, computing time and storage requirements with different algorithms. Table 2 displays the results of region-averaged fluxes. Both M-NEFD and APSN-NEFD can provide accurate results. M-NEFD gives a -0.082% eigenvalue error, while APSN gives a smaller 0.007% eigenvalue error. All the region-averaged flux errors are within 0.56% for the two algorithms. Almost equal computing time and storage are used by the two options. Due to the extra CPU time for projection relation preprocessing and Eq. (54) implementation during iteration and the extra storage for the relation table, APSN-NEFD doesn't show advantages as for computing time and storage requirements for this problem with small void regions.

3.2. A fixed-source problem with one large void region

This problem is a 3-D fixed-source problem with three regions as illustrated in Fig. 6. The inner source region is a $10 \times 10 \times 10$ cm^3 cuboid. The void region is a $90 \times 90 \times 90$ cm^3 cuboid excluding the source region. The outer shell is a shielding region. One energy group macroscopic cross sections are provided. For the source and shielding regions, the total cross section is 0.1 cm^{-1} and the scattering cross section is 0.05 cm^{-1}. The source intensity is 1.0 cm^{-3}s^{-1}. Reflective boundary conditions are used on the left (OCGE), near (OBFE), bottom (OBDC) boundaries, while vacuum boundary conditions for the other three boundaries.

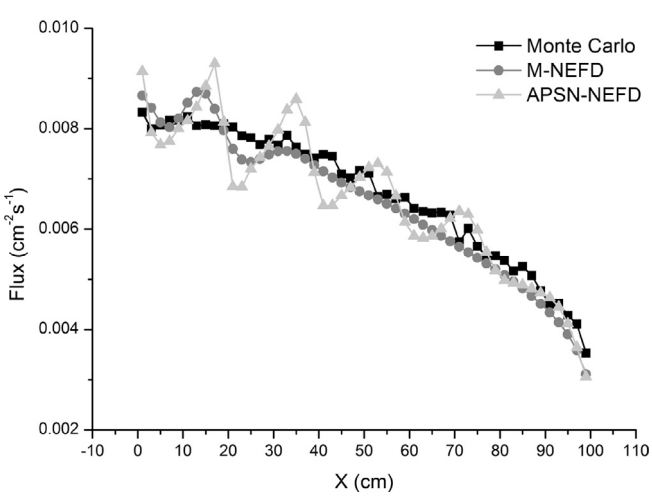

Fig. 7. Flux distribution along boundary line GH.

S_{32} Legendre-Chebyshev quadrature was used to minimize the ray effect, the expansion orders of interior flux and source are 1, while the nodal dimensions are 2 cm with one CPU processor employed. For APSN-NEFD, the void region is approximated by one $80 \times 88 \times 88$ cm^3 cuboid and one $6 \times 88 \times 80$ cm^3 cuboid. Table 3 displays the results of region-averaged fluxes and their errors, CPU time and storage requirements with different algorithms. The errors in the source region given by both M-NEFD and APSN-NEFD are 0.03%. For the shielding region, M-NEFD gives a 0.51% error, while APSN-NEFD gives a smaller 0.11% error. Fig. 7 shows the flux distributions on the boundary line GH obtained by different algorithms. The flux distribution errors of both algorithms are obvious due to the strong ray effect and M-NEFD gives less fluctuant result due to the cancellation of the flux-averaging effect and the ray effect as analysed in Section 2.4. In terms of CPU time, M-NEFD spends 637.8 s in total while APSN-NEFD spends 300.3 s in total, 53% less than the former. For M-NEFD, the iteration time is 636.2 s and the setup time is nearly zero. For APSN-NEFD, the iteration time is 219.8 s and the setup time is 79.9 s. The storage requirement of M-NEFD is 11.9 GB while that of APSN-NEFD is 4.8 GB, 60% less than the former mainly due to the fact that there is no need to store the nodal response information for void nodes. Although 66% of void-nodal sweeps are eliminated by the APSN option, extra CPU time is required to process the relation table in the setup stage and to implement Eq. (54) in the iteration stage, and extra storage is needed to store the relation table.

4. Conclusions

Improvements have been made to the discrete nodal transport method (DNTM) for solving neutron transport problems with void regions in 3-D Cartesian geometry. The effective nodal-equivalent finite difference (NEFD) algorithm has been investigated, singularity of void nodes was found in NEFD equations due to the appearance of total cross section in the denominator. The NEFD equations were modified, named M-NEFD, to directly sweep the void nodes by removing the total cross section to the integration coefficients. A complete form of the integration coefficients considering zero total cross section was derived. As a further research, a new algorithm named APSN-NEFD (angle projection discrete-ordinates - NEFD) was developed to treat problems with large void regions. It eliminates void-nodal sweeps by using a pre-evaluated relation table of the void boundary nodal-surface fluxes.

A 3-D nodal-transport code named NECP-HONESTY was developed using the M-NEFD algorithm and the APSN method as options to treat problems with void regions. A 3-D fission-source problem with two small void regions and a 3-D fixed-source problem with one large void region were presented in this paper to test the new code. In terms of eigenvalue and region-averaged fluxes, both M-NEFD and APSN-NEFD can give accurate results compared with Monte Carlo method. And APSN-NEFD can efficiently reduce the

computing time and storage requirements for problem with large void regions.

Both M-NEFD and APSN-NEFD can be used to treat fission-source problems with void regions. Although the APSN method can expose the ray effect observed in this paper, elimination of void-nodal sweeps will make it possible for direct reactor building calculation and other applications with large void regions. Further work to eliminate the ray effect of the APSN method is expected.

Acknowledgements

This work was financially supported by the National Natural Science Foundation of China (11475134 and 11522544) and China General Nuclear Power Group. In addition, the first author wants to express his appreciation to Prof. Wei Shen from Canadian Nuclear Safety Commission for proofreading this paper, and to Chao Fang, Yunlong Xiao, Tengfei Zhang, Mingtao He, Bin Zhang and Liang Liang for their help during processes of the theoretical derivation, code development and verification.

References

Azmy, Y.Y., 1988. The weighted diamond-difference form of nodal transport methods. Nucl. Sci. Eng. 98, 29–40.

Badruzzaman, A., 1985. An efficient algorithm for nodal-transport solutions in multidimensional geometry. Nucl. Sci. Eng. 89 (3), 281–290.

Badruzzaman, A., Xie, Z., 1984. A three-dimensional linear nodal transport method. Trans. Am. Nucl. Soc. 47, 223–224.

Chapman, B., Jost, G., Van, D.P.R., 2007. Using OpenMP: Portable Shared Memory Parallel Programming. The MIT Press.

He, M., Wu, H., et al., 2015. Beam transient analyses of accelerator driven subcritical reactors based on neutron transport method. Nucl. Eng. Des. 295, 489–499.

Ikeda, H., Takeda, T., 1994. A new nodal S_N transport method for three-dimensional hexagonal geometry. J. Nucl. Sci. Technol. 31 (6), 497–509.

Lawrence, R.D., 1986. Progress in nodal methods for the solution of the neutron diffusion and transport equations. Prog. Nucl. Energy 17 (3), 271–301.

R.D. Lawrence, J.J. Dorning, 1980. A discrete nodal integral transport-theory method for multidimensional reactor physics and shielding calculations. In: Proc. Of ANS meeting 1980 Advances in Reactor Physics and Shielding, Sun Valley, Idaho, September 14–17, 1980.

Lu, H., Wu, H., 2007. A nodal S_N transport method for three-dimensional triangular-Z geometry. Nucl. Eng. Des. 237 (8), 830–839.

Preparata, F.P., Shamos, M.I., 1985. Computational Geometry: An Introduction. Springer-Verlag, New York, Inc.

Takeda, T., Ikeda, H., 1991. "3-D Neutron Transport Benchmarks", OECD/NEA Committee on Reactor Physics (NEACRP), NEACRP-L-330. OSAKA University, Japan.

Takeda, T., Yamamoto, T., 2001. Nodal transport methods for XYZ and hexagonal-Z geometry. Transp. Theor. Stat. Phys. 30 (4–6), 401–420.

Walters, W.F., 1986. Augmented weighted-diamond form of the linear-nodal scheme for cartesian coordinate systems. Nucl. Sci. Eng. 92 (2), 192–196.

Wu, H., Xie, Z., Zhu, X., 1994. The nodal discrete-ordinate transport calculation of anisotropy scattering problem in three-dimensional cartesian geometry. Nucl. Power Eng. 15 (2), 138–142.

Xiao, Y., Wu, H., et al., 2015. Neutronics studies on the feasibility of developing fast breeder reactor with flexible breeding ratio. J. Nucl. Sci. Technol. 53 (1), 1–10.

Zhou, S., Wu, H., et al., 2014. LAVENDER: a steady-state core analysis code for design studies of accelerator driven subcritical reactors. Nucl. Eng. Des. 278, 434–444.